Long-range magnetic order in CePdAl₃ enabled by orthorhombic deformation

M. Stekiel [1,2,*] P. Čermák,[1,3] C. Franz [1,4] M. Meven [1,5] D. Legut [3,6] W. Simeth [2] U. B. Hansen [7]
B. Fåk,[7] S. Weber,[2] R. Schönmann,[2] V. Kumar,[2] K. Nemkovski [1,8] H. Deng,[1,5,†] A. Bauer [2,9]
C. Pfleiderer [2,4,9,10] and A. Schneidewind [1]

[1]*Jülich Centre for Neutron Science (JCNS) at Heinz Maier-Leibnitz Zentrum (MLZ),*
Forschungszentrum Jülich GmbH, Lichtenbergstrasse 1, 85747 Garching, Germany
[2]*Physik-Department, Technische Universität München (TUM), James-Franck-Strasse 1, 85748 Garching, Germany*
[3]*Charles University, Faculty of Mathematics and Physics,*
Department of Condensed Matter Physics, Ke Karlovu 5, 121 16 Praha, Czech Republic
[4]*TUM at MLZ, Lichtenbergstrasse 1, 85748 Garching, Germany*
[5]*Institute of Crystallography, RWTH Aachen University, 52056 Aachen, Germany*
[6]*IT4Innovations, VŠB-Technical University of Ostrava, 17 Listopadu 2172/15, 708 00 Ostrava, Czech Republic*
[7]*Institut Laue-Langevin, 71 Avenue des Martyrs, 38042 Grenoble, France*
[8]*ISIS Neutron and Muon Source, STFC Rutherford Appleton Laboratory, Harwell Campus, Didcot, Oxon OX11 0QX, United Kingdom*
[9]*Center for Quantum Engineering, TUM, 85748 Garching, Germany*
[10]*Munich Center for Quantum Science and Technology, TUM, 85748 Garching, Germany*

We investigate the effect of structural deformation on the magnetic properties of orthorhombic CePdAl₃ in relation to its tetragonal polymorph. Utilizing x-ray and neutron diffraction, we establish that the crystal structure has the *Cmcm* space-group symmetry and exhibits pseudotetragonal twinning. According to density functional calculations, the tetragonal-orthorhombic deformation mechanism has its grounds in the relatively small free enthalpy difference between the polymorphs, allowing either phase to be quenched, and fully accounts for the twinned microstructure of the orthorhombic phase. Neutron diffraction measurements show that orthorhombic CePdAl₃ establishes long-range magnetic order below $T_N = 5.29\,(5)$ K characterized by a collinear, antiferromagnetic arrangement of magnetic moments. Magnetic anisotropies of orthorhombic CePdAl₃ arise from strong spin-orbit coupling as evidenced by the crystal-field splitting of the $4f$ multiplet, fully characterised with neutron spectroscopy. We discuss the potential mechanism of frustration posed by antiferromagnetic interactions between nearest neighbors in the tetragonal phase, which hinders the formation of long-range magnetic order in tetragonal CePdAl₃. We propose that orthorhombic deformation releases the frustration and allows for long-range magnetic order.

I. INTRODUCTION

Symmetry is a fundamental characteristic of any physical system, determining the presence of certain properties and their anisotropy [1]. For crystalline compounds, where the crystal structure reflects the symmetry of the system, determining the structure-property relations is of fundamental importance for understanding emerging phenomena and

___

*m.stekiel@fz-juelich.de

†Present address: School of Physical Science and Technology, ShanghaiTech University, Shanghai 201210, China, ShanghaiTech Laboratory for Topological Physics, ShanghaiTech University, Shanghai 201210, China.

tailoring materials with desired functionalities. In particular, the class of ternary intermetallics with the ThCr₂Si₂ parent structure comprises hundreds of members [2], among which there are systems that exhibit compelling properties such as unconventional superconductivity [3–7], heavy-fermion states [8–10], non-Fermi-liquid behavior [11], and complex magnetic order [12–17].

Here, we investigate CeTX_3 systems, the Ce-113 family, where T is a transition metal and X is a p-block element. We focus on the long-range magnetic order, which emerges as a combination of single-ion anisotropies and exchange interactions of cerium $4f$ electrons. The crystal-electric field (CEF) splits the $4f$ multiplet introducing single-ion anisotropies [18], while exchange interactions typically emerge from indirect interaction between f electrons mediated by the conduction band formalized as Rudermann-Kittel-Kasuya-Yosida (RKKY) interaction [19]. Our scientific interest is driven by the observation of multiple types of magnetic modulations in members of the Ce-113 family sharing the same crystal structure, described with the tetragonal $I4mm$ space group.

Despite structural identity, the types of magnetic order include amplitude [12,15,20–22] and spatial modulations [13,14], with the moments along the fourfold axis [20–22] or perpendicular to it [12,13,21]. In addition, the tetragonal $CePdAl_3$ member of the family was reported to defy long-range magnetic ordering down to 0.1 K [23], and presents itself as an interesting candidate to study the components required to establish and characterize long-range magnetic order in the Ce-113 family.

Previous reports on the magnetic properties of $CePdAl_3$ are based on specific heat, magnetization, magnetic susceptibility, and resistivity measurements as a function of temperature and applied field [23–25]. They conclude that the tetragonal variant of $CePdAl_3$ with the *I4mm* space group does not exhibit long-range magnetic order down to 0.1 K [23,24]. However, the orthorhombic variant of $CePdAl_3$, obtained by a modified synthesis protocol, shows features that are characteristic of long-range magnetic ordering at low temperature [24,25]. In particular, the specific heat exhibits a broad transition at $T_{N_1} = 5.6$ K and a λ anomaly at $T_{N_2} = 5.4$ K. Magnetic properties of orthorhombic $CePdAl_3$ are characteristic of an easy-axis antiferromagnet (AF), in which the ground-state multiplet of the $4f$ electron is split into three doublet states [25].

In this study, we report on the crystal and magnetic structure of orthorhombic $CePdAl_3$ as well as the characterization of the $4f$ multiplet split by the crystal-electric field. The samples studied here originate from the same synthesis batch as in Ref. [25], where the system was characterized by means of specific heat, magnetic susceptibility, and magnetization under applied field down to 2 K. Parts of this study, specifically the twinning scheme and lattice type drawn from x-ray diffraction measurements, were reported in Ref. [25]. Here, we elaborate further on these aspects, together with a precise report on the space-group assignment, as well as the crystal structure solution and refinement. Based on density functional theory (DFT) calculations, we investigate the structural stability of the tetragonal and orthorhombic polymorphs of $CePdAl_3$. We report a neutron diffraction study at low temperature and identify a long-range magnetic order with a collinear, antiferromagnetic arrangement of magnetic moments. Based on inelastic neutron scattering measurements, we determine the CEF scheme utilizing tools specifically developed to analyze the measured data. This approach to data analysis allows one to constrain the parameters describing the crystal-electric field in orthorhombic $CePdAl_3$ and determine a unique set of parameters. The characteristics of the orthorhombic $CePdAl_3$ determined by various techniques in this and the related study [25] provide a consistent picture of the structural and magnetic properties of the system.

II. METHODS

A. Sample synthesis and characterization

Orthorhombic $CePdAl_3$ was grown in an optical furnace utilizing the floating-zone technique [26,27]. The synthesis protocol is described in Ref. [25]. Crystals from the same rod were used to perform measurements described in Ref. [25], where they were thoroughly characterized by means of specific heat, magnetization, and ac susceptibility measurements.

According to the experimental technique, samples of specific size were extracted from the crystalline rod. X-ray diffraction measurements were performed on six crystals with cuboid shape and dimensions varying between 10 and 50 μm. Neutron diffraction measurements were conducted on a cuboid-shaped crystal with dimensions $1 \times 2 \times 4$ mm^3. Neutron spectroscopy measurements were performed with a cylinder-shaped crystal with diameter of 6 mm and length 15 mm.

B. X-ray and neutron scattering

X-ray diffraction measurements were performed on a Rigaku XtaLAB Synergy-S diffractometer, using a Mo x-ray source providing a monochromatic beam with a wavelength of 0.71 Å and a two-dimensional HyPix-Arc 150° detector. The observed reflections were indexed and integrated using the data reduction program CRYSALISPRO [28].

The modulation vector of the magnetic order in $CePdAl_3$ was determined from measurements at the Diffuse Neutron scattering Spectrometer (DNS) [29,30] at Heinz Maier-Leibnitz Zentrum (MLZ) using polarization analysis. The incoming neutron's wavelength was 4.2 Å covering the momentum transfer range Q of $0.25 < Q < 2.7$ Å^{-1}. The sample was rotated in 1° steps in a 140° range to map the neutron scattering intensity. The incoming neutrons were polarized along the momentum transfer vector, which allows one to distinguish between magnetic and nuclear scattering contributions on the spin-flip (SF) and non-spin-flip (NSF) channels, respectively [30,31]. The flipping ratio for our measurements is FR = 18, which corresponds to the polarization efficiency $\epsilon = 95\%$. The data were analyzed, reduced, and corrected for flipping ratio using the MANTID package [32].

Intensities of the nuclear and magnetic reflections required to determine the type of long-range magnetic order in $CePdAl_3$ were measured at the neutron diffractometer HEiDi [33] at MLZ. The crystal was mounted on an Eulerian cradle; the wavelength of incoming neutrons was 0.793 Å. Scattered neutrons were measured by a point detector moving in the horizontal plane. First, the sample was measured at ambient conditions and then it was mounted in a closed cycle cryostat. A series of measurements was performed at various temperatures down to 2.4 K. Intensities of the observed reflections were refined with the JANA program [34].

The excitation spectrum of the $4f$-electron split in the crystal field of orthorhombic $CePdAl_3$ was determined from measurements at the thermal neutron time-of-flight spectrometer PANTHER [35] at the Institut Laue-Langevin. The instrument operates with a single-crystal monochromator and a Fermi chopper, which provide a monochromatic beam of incoming neutrons at required energies. An array of ^{3}He tubes forms a 2D position-sensitive detector covering 141° in-plane and 43° out-of-plane scattering angles.

C. Density functional theory calculations

The calculations were performed within the density functional method implemented in the Vienna *Ab Initio* Simulation package [36]. We employed projector augmented-wave pseudopotentials utilizing the generalized gradient

approximation exchange-correlation functional with the Perdew, Burke and Ernzerhof parametrization [37].

The electronic valence configurations for Ce, Pd, and Al were $6s^2 5d^1 4f^1$, $5s^1 4d^9$, and $3s^2 2p^1$, respectively. The Brillouin zone was sampled with 245 and 220 k points for the orthorhombic *Cmcm* and tetragonal *I4mm* phases, respectively, and a plane-wave energy cutoff of 480 eV was used for both.

Structures were fully optimized, including lattice parameters and atomic positions, for selected volumes. Convergence criteria for total energy and forces acting on each atom were set at less than 10^{-7} eV and 10^{-5} eV/Å, respectively.

The dynamical properties of the orthorhombic and tetragonal lattices were investigated using the quasiharmonic approximation for lattice vibrations on a $2 \times 2 \times 2$ supercell, employing PHONOPY [38]. This allowed determination of the phonon density of states and, subsequently, the thermodynamic properties, such as the Gibbs free energy, including the electronic contribution as a function of temperature. The transition temperature was determined similarly to recent work; see Ref. [39] and references therein for details.

D. Crystal-electric field transitions

The crystal-electric field lifts the degeneracy of the $4f$ multiplet and splits the energy levels on scales typically accessible with neutron scattering. The good quantum number describing this problem is the total angular momentum J, and the analysis follows from considering the CEF Hamiltonian,

$$\hat{H} = \sum_{n,m} B_n^m \hat{O}_n^m. \qquad (1)$$

Here, $\hat{O}_n^m$ are Stevens operators and B_n^m are crystal-field parameters. Stevens operators consist of total momentum operators $\hat{J}_x, \hat{J}_y, \hat{J}_z$ grouped, raised to the power n, and composed in a way that reflects the point symmetry of the magnetic ion [18]. Additionally, symmetry restrictions can constrain the values of some B_n^m parameters to zero. The Hamiltonian from Eq. (1) represented in the $|m_J\rangle$ basis, where $m_J = J, J - 1, \ldots, -J$, is diagonalized and the eigenstates $|\lambda\rangle$ are linear combinations of the $|m_J\rangle$ states.

The cross section of the neutron scattering process corresponding to the CEF transition from state $|\lambda_i\rangle$ to $|\lambda_f\rangle$ for neutron momentum transfer $\boldsymbol{Q}$ and energy transfer E follows from the expectation values of the perpendicular projection of the total momentum operator $\hat{\boldsymbol{J}} = (\hat{J}_x, \hat{J}_y, \hat{J}_z)$ on the momentum transfer [31]. This is expressed as

$$\frac{d\sigma}{d\Omega} \propto |\langle \lambda_f | \hat{\boldsymbol{J}}_{\perp Q} | \lambda_i \rangle|^2$$
$$= \sum_\alpha [1 - (Q_\alpha/|\boldsymbol{Q}|)^2] |\langle \lambda_f | \hat{J}_\alpha | \lambda_i \rangle|^2, \qquad (2)$$

where α indexes the Cartesian components, $\alpha = x, y, z$.

Expression (2) can be conveniently evaluated for polycrystalline samples, where the momentum transfer $\boldsymbol{Q}$ is angularly averaged, yielding $\frac{2}{3} \sum_\alpha \langle \lambda_f | \hat{J}_\alpha | \lambda_i \rangle|^2$. However, this approach would result in a loss of information, providing fewer constraints for determining the crystal-field parameters.

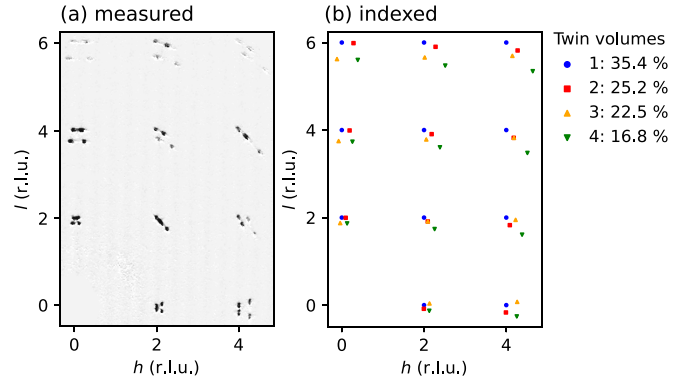To address this limitation, we have developed tools to directly evaluate Eq. (2) for any measured $Q - E$ point. This

FIG. 1. Diffractogram of orthorhombic CePdAl₃. (a) Measured x-ray scattering intensity reconstructed on the $(h0l)$ plane in reciprocal space. (b) Indexing of reflections from (a), with four identical, orthorhombic lattices grouped by color. Indices follow the majority twin (blue circles). The characteristic splitting of reflections reveals pseudotetragonal twinning.

allows us to qualitatively analyze neutron scattering intensity due to CEF transitions on a single-crystal sample and impose stronger constraints on the B_n^m parameters. The code used in the analysis is available under the public repository CRYSFIPY [40], developed as an extension of the previous version of the project [41].

For the case of a cerium atom with $J = \frac{5}{2}$ that exhibits $m2m$ (C_{2v}) point symmetry, there are five nonzero B_n^m parameters. At the same time, $J = \frac{5}{2}$ signifies a Kramers' ion, and in this case, the CEF energy level scheme consists of three doublet states. The standard method of analyzing the transition energies and transition intensity ratio on a polycrystalline sample would yield only three constraints, while our method provides additional ones.

III. EXPERIMENTAL RESULTS

A. Pseudotetragonal twinning

Here, we elaborate on details of our recent study [25] and present an extended analysis of the twinning and crystal structure determination.

We investigated the x-ray diffraction pattern of six micrometer-sized crystals of CePdAl₃ at ambient conditions. All patterns consist of a characteristic set of split reflections, as shown in Fig. 1. By indexing measured reflections, we disentangle split and overlapped spots into four twins of the same orthorhombic lattice with parameters $a = 6.3785$ (6) Å, $b = 10.402$ (2) Å, and $c = 5.972$ (2) Å. Based on reflection conditions, the diffraction symbol is C-c-, which, following crystallographic convention, establishes b as the long axis.

The characteristic diffraction pattern with sets of three spots around the $(h0h)$ reflections and four spots around the $(h0l)$ $(h \neq l)$ reflections is indicative of pseudotetragonal twinning with diagonal mirror planes defining the twinning laws, as shown in Fig. 2. The relative orientation of all twins follows from the mismatch angle ϕ_m, defined as the angle between close-lying, equivalent axes, such as a_1 and a_2 in Fig. 2(d). Taking the twin with index 1 as the reference, twin 2 is related to twin 1 by a right-handed rotation of an angle
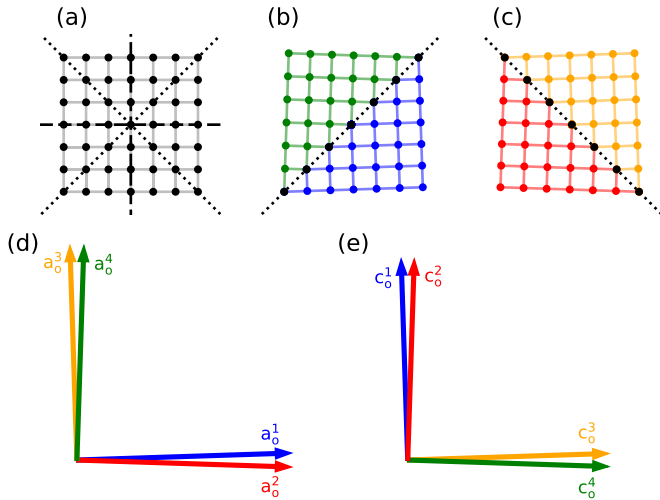
FIG. 2. Twinning scheme in orthorhombic CePdAl₃. (a) Undistorted lattice. Diagonal mirror planes are indicated with dotted lines, normal mirror planes with dashed lines. (b) Twins related by one diagonal mirror plane and (c) the other diagonal mirror plane. (d) Orientation of the (1 0 0) and (e) the (0 0 1) lattice vectors among twins. The scale of the distortion in the figures is the same as determined from the single-crystal x-ray diffraction measurements.

$-\phi_m$ around the perpendicular b axis, twin 3 by rotation of 90°, and twin 4 by rotation of $90 - \phi_m$. The mismatch angle determined from the orientation matrices is $\phi_m = 3.7(3)°$.

Despite pseudotetragonal symmetry, the twin volumes are not equal. Instead, in the crystal selected for structure determination, twins 1 and 2 represent 35.4% and 25.2% of the crystal volume, respectively, while twins 3 and 4 represent 22.5% and 16.8%, respectively. Other crystals had similar twin volumes, with differences less than 4% for any twin component. This has important consequences for the anisotropic properties, which was taken into account in Ref. [25].

B. Crystal structure

Extinction conditions are characteristic of the symbol $C\text{-}c\text{-}$, for which possible space groups are the centrosymmetric *Cmcm* (No. 63), as well as noncentrosymmetric *Cmc*2₁ (No. 36), and *C*2*cm* (No. 40). A significant amount of overlapping reflections does not allow for a reliable determination of the Flack parameter or directly verify the presence of inversion symmetry.

Crystal structure determination of CePdAl₃ by direct methods results in the PbSbO₂Cl structure type, also reported for the related CeAgAl₃ [23]. The atomic arrangement of the orthorhombic CePdAl₃ is shown in Fig. 3, with detailed parameters in Table I.

Refinement of the measured intensities within the space group *Cmcm* corroborates the structure solution by low R factors, of $R_{\text{int}} = 4.92$ for the data quality, and $R_{\text{obs}} = 3.90$ for the refinement quality. Following the observation of atomic disorder in tetragonal CeTAl₃ systems [14,23], we (i) split the atomic positions of the Pd or Al atoms and (ii) introduced occupational disorder between the Pd and Al sites. Neither (i), (ii), nor a combination of both improved the quality of the refinement.
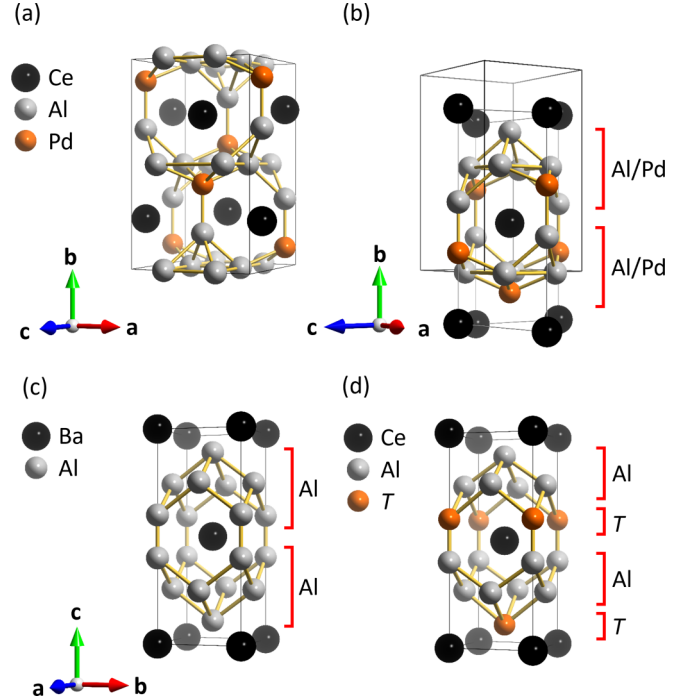

FIG. 3. Crystal structure of orthorhombic CePdAl₃ and related compounds. *Cmcm* structure of CePdAl₃ with atoms (a) in the orthorhombic unit cell and (b) projected to the tetragonal unit cell. (c) Centrosymmetric, tetragonal BaAl₄ structure with space group *I*4/*mmm*. (d) Noncentrosymmetric, tetragonal CeTAl₃ structure with *I*4*mm* space group. Note the increasing level of distortion in the neighborhood of the cerium atom in the *I*4/*mmm* → *I*4*mm* → *Cmcm* series. Red brackets enclose atoms forming uni-atomic layers in (c) and (d), and mixed Al-Pd layer in CePdAl₃. The unit cell is marked with a solid black line; close-lying atoms are connected with yellow lines.

TABLE I. Details of the orthorhombic CePdAl₃ crystal structure based on refinement of x-ray diffraction data at ambient temperature. Space group *Cmcm*, $a = 6.3785(6)$ Å, $b = 10.402(2)$ Å, $c = 5.972(2)$ Å. The number of measured, independent, and observed reflections is 2509, 280, and 260, respectively. The reflection merge factor $R_{\text{int}} = 4.92$; observed reflections are with $I > 3\sigma(I)$. The refinement was performed on F^2 with $R_{\text{obs}} = 3.90$ and $wR_{\text{obs}} = 8.47$. The columns contain the name of the elements, Wyckoff site symbols, atomic coordinates, and displacement parameters, respectively. Numbers without errors are restricted by symmetry.

Element	Site	Position	U (Å²)
Ce	4*c*	$x = 0$	$U_{11} = 0.0313(5)$
		$y = 0.7647(1)$	$U_{22} = 0.0275(5)$
		$z = 0.25$	$U_{33} = 0.0333(5)$
Pd	4*c*	$x = 0$	$U_{11} = 0.0317(6)$
		$y = 0.0949(1)$	$U_{22} = 0.0285(7)$
		$z = 0.25$	$U_{33} = 0.0392(7)$
Al	4*c*	$x = 0$	$U_{11} = 0.0257(19)$
		$y = 0.3336(5)$	$U_{22} = 0.0400(30)$
		$z = 0.25$	$U_{33} = 0.0251(18)$
Al	8*e*	$x = 0.2795(5)$	$U_{11} = 0.0309(15)$
		$y = 0$	$U_{22} = 0.0289(17)$
		$z = 0$	$U_{33} = 0.0328(15)$
			$U_{23} = 0.0008(12)$

Another attempt to model disorder was made by considering the noncentrosymmetric space groups $Cmc2_1$ and $C2cm$, as they lift constraints on certain atomic positions. The refinement quality factors do not differ significantly, $R_{obs}^{Cmc2_1} = 3.93$, $R_{obs}^{C2cm} = 3.71$, despite introducing additional parameters. The shifts of the atomic positions are smaller than 0.03 Å with respect to the $Cmcm$ model.

An independent investigation of the crystal structure was based on neutron diffraction measurements. Large data sets were collected at 300 and 10 K; each contains a few-hundred reflections. Refinements result in the same crystal structure as described in Table I with negligible differences in atomic positions, which are smaller than 1% of the relative difference.

In conclusion, we describe the crystal structure of orthorhombic CePdAl$_3$ with the highest symmetry suitable space group $Cmcm$ and atomic coordinates listed in Table I, without evidence of atomic disorder.

The description of the crystal structure is facilitated by comparing it with the tetragonal $I4mm$ structures of CeTAl$_3$, T = Cu, Au, Pt [23], and the ThCr$_2$Si$_2$ aristotype represented by BaAl$_4$ with $I4/mmm$ space group [42], shown in Fig. 3. In those compounds, the crystal structure consists of a three-dimensional X-Al network, where X is either T or Al, forming cages occupied by the central Ce atom.

In the high-symmetry BaAl$_4$ structure, the cerium atoms are neighbored by aluminium atoms, as shown in Fig. 3(c). By removing the inversion symmetry, the $I4/mmm$ structure transforms into the CeTAl$_3$ type [see Fig. 3(d)], adapted by tetragonal CePdAl$_3$. In this configuration, cerium atoms are surrounded on one side by T atoms and on the other by aluminium atoms, forming uni-atomic layers, highlighted in Fig. 3.

Alternatively, orthorhombic distortion of the BaAl$_4$ structure and further splitting of the atomic position results in the $Cmcm$ structure, adapted by orthorhombic CePdAl$_3$. The inversion symmetry is preserved, but with respect to the corners of the orthorhombic unit cell, where no atom resides. As a result, the environment of the cerium atom in the $Cmcm$ structure is more distorted than in CeTAl$_3$ [compare Figs. 3(b) and 3(d)] and the layers between the cerium atoms are comprised of mixed palladium and aluminium atoms.

C. Structural stability of the orthorhombic phase

In order to verify the thermodynamic stability of the orthorhombic CePdAl$_3$, we investigated its Gibbs free energy G as a function of temperature. As an alternative structure, we considered the tetragonal $I4mm$ variant, reported by [23] and depicted in Fig. 3(d).

The Gibbs free energy as a function of temperature is shown in Fig. 4. The phases have equal energy at $T_{crit} = 297$ K, which marks the structural transition temperature between the $I4mm$ and $Cmcm$ structures. Above T_{crit}, the tetragonal phase has lower energy and is thus stable, while the orthorhombic phase is metastable. Below T_{crit}, the situation is reversed and the orthorhombic variant is thermodynamically stable.

The difference in Gibbs energy, ΔG, between those phases is relatively small, i.e., less than 1 kJ/mol in the studied temperature range; see Fig. 4(b). Our calculations do not de-
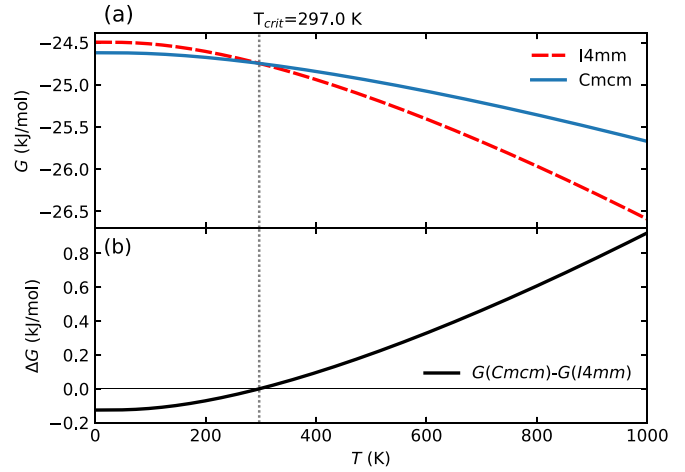

FIG. 4. Gibbs free energy G of the structural variants of CePdAl$_3$. (a) G as a function of temperature for the tetragonal $I4mm$ (dashed red line) and orthorhombic $Cmcm$ (solid blue line) variants. (b) Difference in G between the orthorhombic and tetragonal variants. The dotted vertical line at $T_{crit} = 297$ K marks the point with $\Delta G = 0$, where a structural transition would occur.

termine the activation energy between the considered phases; however, this should be relatively high, given the displacive character of the transition, which involves rearrangement of the Al-Pd atomic positions, as depicted in Figs. 3(b) and 3(d). These observations suggest that both phases can exist at ambient conditions, either in a stable or metastable form, consistent with previous reports [23–25].

D. Magnetic structure

Orthorhombic CePdAl$_3$ shows two magnetic transitions at low temperatures, at $T_{N_1} = 5.6$ K and $T_{N_2} = 5.4$ K [25]. In order to determine the type of magnetic order, we performed a series of neutron diffraction measurements.

Mapping of the reciprocal space of CePdAl$_3$ by neutron scattering at 3 K, below the magnetic transitions, is shown in Fig. 5. Reflections are separated based on the nuclear or magnetic origin owing to polarization analysis, as shown in Figs. 5(a) and 5(b), respectively.

Some reflections are split or misaligned with respect to the indices of the majority twin, indicated by the grid. The map of nuclear reflections expected for the $Cmcm$ space group within the twinning scheme described in Sec. III A is shown in Fig. 5(c), and is fully consistent with the observed reflections as shown in Fig. 5(a).

Taking twinning into account, all magnetic reflections occur at integer positions, indicating a commensurate magnetic structure, with the magnetic unit cell of the same size as the chemical unit cell. In particular, the magnetic reflection around the $(hk0)_1 = (1 + \delta 00)$ position, identified as the (001) reflection from twins 3 and 4, is not allowed by the extinction rules of the $Cmcm$ space group, and is indicative of an antiferromagnetic order with magnetic moments alternating along the (001) planes.

The development of the magnetic order parameter was followed by single-crystal neutron diffraction measurements. Rocking scans and integrated intensities of the (001)
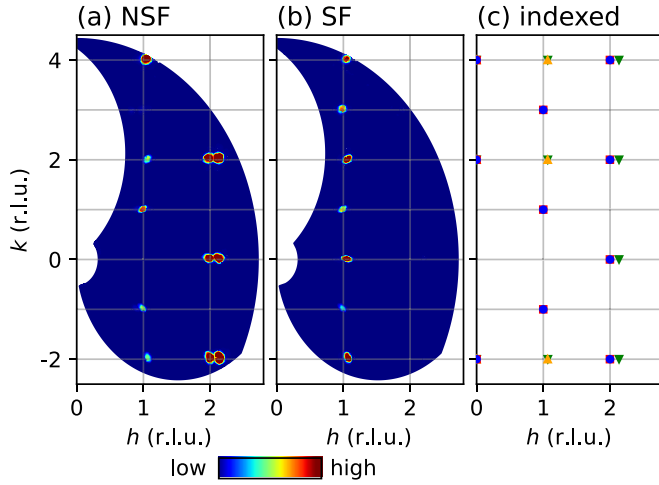
FIG. 5. Neutron scattering intensity in the $(hk0)$ plane of CePdAl$_3$ at 3 K. (a) Intensity of the non-spin-flip (NSF) channel, where nuclear Bragg reflections are observed, and (b) in the spin-flip channel (SF), where magnetic reflections are visible. (c) Splitting and misalignment of nuclear reflections, as inferred from the twinning. Only reflections allowed by the *Cmcm* space group are shown in (c), with the indexation scheme as in Fig. 1.

reflection, with purely magnetic contribution, are shown in Fig. 6(a). The (001) reflection is split, as a consequence of the misalignment between the twins indexed 3 and 4. The integrated intensity exhibits a sharp drop for increasing temperature. It closely follows the order parameter modeled by the function $I \propto (1 - T/T_N)^\beta$, as indicated by the solid line in Fig. 6(b). The fit of the order parameter to the intensity of the (001) reflection, as well as five other magnetic reflections (not shown), leads to a transition temperature $T_{\mathrm{N}} = 5.289\,(51)$ K and $\beta = 0.488\,(44)$ for the critical exponent.

The value determined here corresponds to the sharp peak in the specific heat at $T_{\mathrm{N}_2} = 5.4$ K, while there is no evidence of any additional feature coinciding with the broad shoulder at $T_{\mathrm{N}_1} = 5.6$ K. However, the neutron diffraction data were
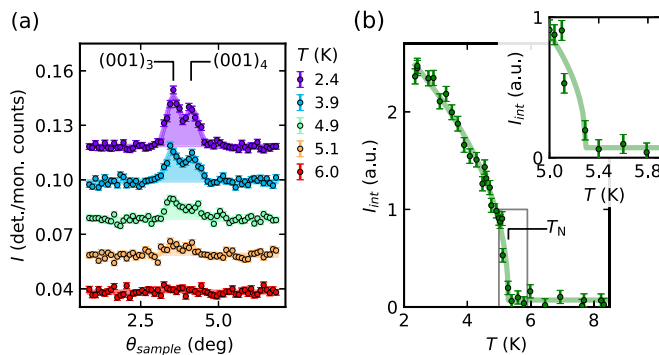

FIG. 6. Development of the magnetic order in CePdAl$_3$. (a) Rocking scans of the $(0\,0\,1)$ reflection at various temperatures. The splitting of the reflection is due to twinning, with the contributing twins marked. Points indicate measured data; lines are guides to the eye. (b) Integrated intensity of the $(0\,0\,1)$ reflection as a function of temperature. The fitted order parameter is shown with a solid line.
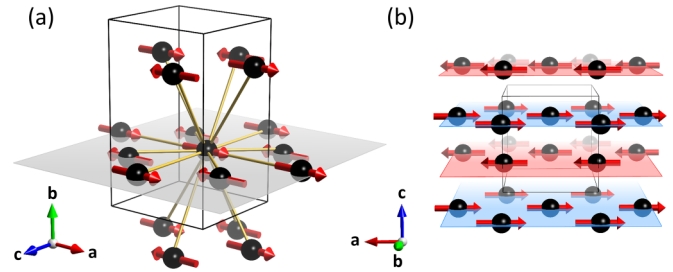

FIG. 7. Magnetic ordering in CePdAl$_3$. Magnetic moments are oriented along the *a* axis in a collinear, antiferromagnetic arrangement. (a) Neighbors of the central cerium atom in the unit cell. The highlighted plane marks the distorted square plane, where four nearest neighbors are aligned in an antiferromagnetic configuration with the central atom and four next-nearest neighbors in a ferromagnetic configuration. In addition, there are eight next-nearest neighbors out of plane, aligned in either an antiferromagnetic or ferromagnetic configuration. (b) Magnetic moments within *ab* planes (highlighted) form ferromagnetic sheets stacked antiferromagnetically along the *c* axis.

recorded with a temperature step of ≈ 0.2 K, which might be too coarse.

The determination of the magnetic order is based on the sets of reflections measured at 10 and 2.4 K. First, atomic positions were refined with the 10 K dataset, with the same results as for the x-ray diffraction measurements listed in Table I. These results were then used as fixed parameters for the refinement of the magnetic structure with the reflections measured at 2.4 K.

The best refinement was obtained with the model described by the *Cmcm'* magnetic space group (No. 63.461). It describes collinear, antiferromagnetic order of magnetic moments located at the Ce sites, oriented along the *a* axis, shown in Fig. 7. This corresponds to ferromagnetic order of the *ab* planes, stacked along the *c* axis, as shown in Fig. 7(c). The refined value of the ordered magnetic moment is $\mu_{Ce} = 1.672\,(72)\,\mu_B$.

E. Crystal-electric fields

The $4f$ multiplet of the cerium atom with total angular momentum $J = 5/2$ consists of six states. In the orthorhombic CePdAl$_3$, the cerium atom is subject to crystal-electric fields with $m2m$ point-group symmetry, which lifts the sixfold degeneracy into three Kramers' doublets, and allows for two CEF excitations from the ground state. The crystal-electric field is characterized by five B_n^m parameters, with eigenvectors and excitation energies determined from Eq. (1).

To investigate the crystal-electric fields in CePdAl$_3$, we performed inelastic neutron scattering (INS) measurements. The measured crystal was oriented with the (hkh) reflections in the scattering plane, a configuration approximately shared among all twin domains, with a mismatch of $3.7°$. Measurements of the crystal in this orientation allow one to determine the spectral weight $S(\mathbf{Q}, E)$, for any vector $\mathbf{Q}$ with (hkh) crystal coordinates.

The momentum-averaged ($|\mathbf{Q}| = Q$) and energy-resolved spectral weight $S(Q, E)$ measured at 10 K is depicted in
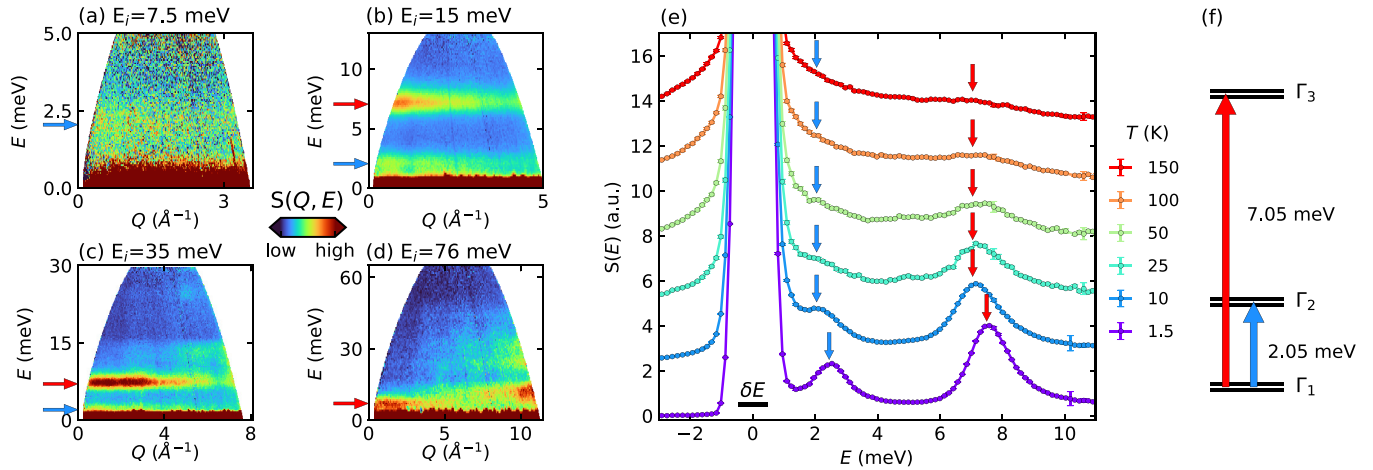
FIG. 8. Inelastic neutron scattering spectra of CePdAl₃. (a)–(d) Spectral weight $S(Q, \omega)$ measured at 10 K with various incoming energies: (a) 7.5 meV, (b) 15 meV, (c) 35 meV, and (d) 76 meV. Two bands of magnetic excitations are identified at positions marked with arrows. (e) Momentum integrated spectral weight $S(\omega)$ measured at various temperatures. Arrows indicate the position of fitted peak centers. Bar around zero corresponds to the instrumental energy resolution of $\delta E = 0.8$ meV as determined from the width of the elastic line at 1.5 K. (f) Sketch of the CEF scheme derived from the measurements and model.

Figs. 8(a)–8(d). In the low-momentum transfers range, $Q < 6$ Å^{-1}, the spectrum exhibits two dispersionless bands of excitations, characterized by a gradual decrease in spectral weight with increasing Q, indicating a magnetic character. As the measurements were performed in the paramagnetic state, well above the magnetic ordering temperature T_N, we interpret them as CEF excitations.

The determination of CEF transition energies is facilitated by examining the momentum-integrated spectral weight, $S(E)$, shown in Fig. 8(e). In this case, the momentum Q was integrated within the range [0.8, 2.2] Å^{-1} with the dataset measured at 10 K and $E_i = 15$ meV as in Fig. 8(b). The excitation energies are found to be $E_1 = 2.05\,(10)$ meV and $E_2 = 7.05\,(3)$ meV at 10 K and at higher temperatures. In the magnetically ordered state at 1.5 K, they shift to $E_1 = 2.41\,(2)$ meV and $E_2 = 7.44\,(2)$ meV, potentially due to internal fields.

In the search for additional constraints on the B_n^m parameters, we have investigated the angular dependence of the spectral weight at the energy transfer in the vicinity of the excitation energy. The characteristic distribution of intensity follows from the expectation value of the $\hat{J}_{\perp Q}$ operator, as in Eq. (2). The energy-integrated spectral weight obtained from measurements at 10 K is shown in Figs. 9(a) and 9(b). These were obtained by integrating $S(\boldsymbol{Q}, E)$ in the ranges [1.5, 3.5] meV and [6, 9] meV, respectively, to capture each transition. Additionally, the angular distribution of the spectral weight for each energy level is displayed in Figs. 9(e) and 9(f). The maps from Figs. 9(a) and 9(b) were radially integrated in the low-Q range [0.75, 1.05] Å^{-1}; $\phi = 0$ corresponds to the $\boldsymbol{Q} = (0k0)$ direction and $\phi = 90°$ to $\boldsymbol{Q} = (h0h)$.

To determine the Stevens parameters B_n^m, we followed the standard procedure employed in the analysis of CEF excitations. In addition, we incorporated constraints derived from the angular distribution of spectral weight for each energy level. The coordinate system for the CEF calculation was taken with quantization axis z along the a crystal axis, y along the b axis, and z along the c axis. We performed a Monte Carlo search of B_n^m parameters, imposing loose constraints on the energy and intensity distribution of the CEF levels. Sets of parameters meeting these constraints were then refined against measured values, with an additional constraint on magnetization such that $M_{c^*} > M_{a^*} > M_{b^*}$ at 12 T, as determined by magnetization measurements [25]. Uncertainties of the B_n^m parameters were estimated from the covariance matrix constructed during the refinement [43].

We tested 10^7 sets of B_n^m parameters, out of which 5.4×10^4 match the measured transition energies and only 826 further match the intensity distribution constraints. For the 826 candidates, refinement converges into two unique sets of B_n^m parameters, which are related to each other by rotating the reference frame by 90° around the y axis, i.e., changing the signs of the B_2^0 and B_2^2 parameters. Such rotation corresponds to exchanging the a and c crystal axes and is consistent with the ambiguity posed by measuring a twinned sample in the (hkh) scattering plane. Finally, we evaluate the ground-state magnetic moment, which is $\pm 1.24\ \mu_B$ for the selected set and $\pm 0.47\ \mu_B$ for the discarded one.

TABLE II. Parameters and eigenvectors of the cerium $4f$ multiplet in the crystal-electric field of orthorhombic CePdAl₃. Each eigenvector is double degenerated, $\Gamma^+ = \alpha\,|\frac{5}{2}\rangle + \beta\,|\frac{3}{2}\rangle + \gamma\,|-\frac{1}{2}\rangle$ and $\Gamma^- = \alpha\,|-\frac{5}{2}\rangle + \beta\,|-\frac{3}{2}\rangle + \gamma\,|\frac{1}{2}\rangle$. Entries list coefficients next to respective ket for either state.

Crystal-field parameters (meV)				
B_2^0	B_2^2	B_4^0	B_4^2	B_4^4
0.224	−0.200	0.01408	−0.0458	0.015
(16)	(27)	(44)	(46)	(10)

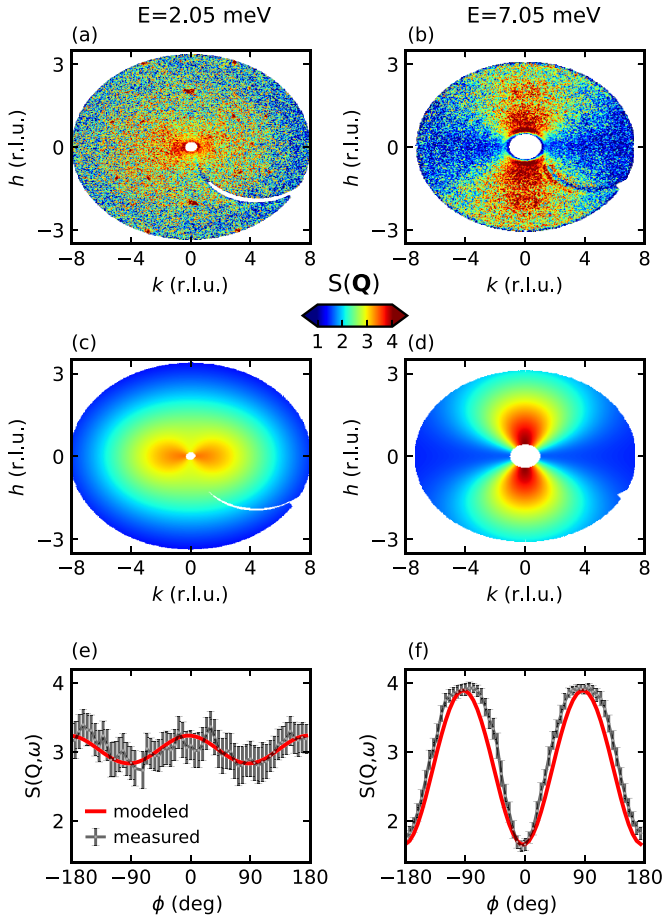| Eigenvectors				
	$|\pm\frac{5}{2}\rangle$	$|\pm\frac{1}{2}\rangle$	$|\mp\frac{3}{2}\rangle$	E (meV)
$\Gamma_1^{\pm}$	0.096	0.105	−0.990	0
$\Gamma_2^{\pm}$	0.415	0.900	0.136	2.05
$\Gamma_3^{\pm}$	0.905	−0.424	0.043	7.05

FIG. 9. Directional dependence of the spectral weight of CEF levels at 10 K. Left column corresponds to the 2.05 meV excitation, right column to the 7.05 meV excitation. (a),(b) Reconstruction of the measured spectral weight in the (*hkh*) plane, obtained by integrating the energy in the vicinity of each level, as described in the main text. (c),(d) Simulated spectral weight, based on parameters from Table II. (e),(f) Radially integrated intensity; comparison between measurement (black points) and simulations (red line). The arc with reduced intensity in the lower-right quadrant of the measured maps is an artifact of the data collection.

The final set of B_n^m parameters is presented in Table II, along with eigenvectors and energy levels characterizing the crystal field in CePdAl$_3$. Remarkably, the energies of the CEF transitions align closely with the observed values, as well as the angular distribution of intensity, shown in Fig. 9.

The eigenvectors show that the ground state is dominated by the $|\pm\frac{3}{2}\rangle$ state, the first excited state by $|\pm\frac{1}{2}\rangle$, and the second excited state by $|\pm\frac{5}{2}\rangle$. The expectation value of the magnetic moment for the ground state is 1.24 μ_B along the quantization axis *a*, close to the value determined from neutron diffraction of 1.67 μ_B.

Finally, we have not observed features characteristic of phonon-CEF coupling [44–46], such as splitting of the CEF transitions in the $S(E)$ reconstruction shown in Fig. 8, or anticrossing causing loss of intensity in $S(\mathbf{Q})$ at the energy of the CEF transition shown in Fig. 9.

IV. DISCUSSION

The combined x-ray and neutron diffraction measurements show that the CePdAl$_3$ sample investigated in this study crystallizes in the *Cmcm* space group, with orthorhombic lattice. It exhibits a pseudotetragonal twinning, suggestive of a high-temperature tetragonal to orthorhombic transition.

For further insights, we examine the synthesis protocols of CePdAl$_3$ from Refs. [23–25]. In particular, Schank *et al.* [24] reports the synthesis of tetragonal CePdAl$_3$ with complete Pd-Al antisite disorder, which, after annealing between 700 and 900 °C, transformed into an unknown phase. The specific heat of this unknown phase shows the same signatures as the orthorhombic CePdAl$_3$ reported by Kumar *et al.* [25] i.e., a sharp λ peak with a shoulder on the high-temperature side. Possibly, after annealing, they obtained the orthorhombic phase of CePdAl$_3$, while their initial synthesis attempt, as well as that of Franz *et al.* [23], resulted in quenching the high-temperature tetragonal phase, which is metastable at ambient conditions. This scenario suggests that the orthorhombic CePdAl$_3$ is thermodynamically stable at ambient conditions, and that it undergoes a structural phase transition from tetragonal to orthorhombic structure between ambient temperature and 1000 K, responsible for the pseudotetragonal twinning.

Our DFT-based calculations of Gibbs energy show that the tetragonal-orthorhombic transition takes place at 297 K. However, the calculations were performed on stoichiometric compounds and without atomic disorder; therefore, the calculations might not accurately depict the thermodynamics of laboratory-grown samples. There seems to be a general tendency of the tetragonal Ce*T*Al$_3$ compounds to exhibit occupational disorder between *T*-Al sites [12,14,47], which might also exist in the tetragonal CePdAl$_3$.

In orthorhombic CePdAl$_3$, the crystal field splits the 4*f* multiplet into three Kramers doublets, as characterized in Table II, with the values closely matching the results of inelastic neutron spectroscopy. The orthorhombic distortion strongly affects the crystal field in CePdAl$_3$, as the constraints of the 4*mm* symmetry exhibited by Ce in tetragonal Ce*T*Al$_3$ systems permit only pure $|\pm\frac{1}{2}\rangle$ states, or mixing between $|\pm\frac{3}{2}\rangle$ and $|\pm\frac{5}{2}\rangle$ states. As reported in Table II, we observe strong mixing between all base states. In addition, the values of the B_2^2 and B_4^2 parameters are zero for 4*mm* symmetry, while we observe relatively large values of those parameters.

The full characterization of the CEF Hamiltonian allows one to derive further observables and compare to the results of Kumar *et al.* [25]. Their analysis of the specific heat shows two CEF contributions at energies of 2.33 (14) and 7.39 (84) meV, consistent with our results. Magnetization measured at 2.4 K shows a kink around 5.5 T that disappears above $T_N = 5.3$ K. The Zeeman energy at 5.5 T is 0.7 meV for the cerium moment, which is not enough to shift the next CEF level (2.05 meV) to the ground state and interpret the kink as a magnetic transition originating solely from CEF effects. Thus, exchange interactions must play a significant role in this field-driven transition. Magnetization saturation values measured at 14 T and 10 K, i.e., at temperature above long-range order where exchange interaction should play a smaller role, are 1.13, 0.75, and 0.43 μ_B along the main

axes, with corresponding calculated values of 1.13, 1.08, and 0.81 μ_B, respectively, providing a good agreement for the model omitting exchange interactions.

The collinear arrangement of the magnetic moments in CePdAl$_3$, as well as the orthorhombic crystal structure, are reminiscent of CeAgAl$_3$, which exhibits ferromagnetic ordering below $T_C = 3.8$ K, and also crystallizes in the *Cmcm* structure [23,48]. The level of distortion in CeAgAl$_3$ quantified from lattice parameters would correspond to a mismatch angle of 0.8°, significantly smaller than 3.7° for CePdAl$_3$.

An interesting observation is that orthorhombic Ce-113 compounds, CePdAl$_3$ and CeAgAl$_3$, establish collinear magnetic order with zero modulation vector, while *all* of the reported tetragonal systems establish nonzero modulation. The modulation is either commensurate, when magnetic moments are aligned with the fourfold axis as in CeTGe$_3$ with T = Rh, Ir, Co [20–22], or incommensurate, when moments are aligned in-plane ($m_z = 0$), as in CeAuAl$_3$ [13], CePtAl$_3$ [14], and CeCuGa$_3$ [15]. An exception from the latter case seems to be posed by CeCuAl$_3$ [12], which establishes in-plane magnetic order with commensurate modulation of five unit cells.

This observation leads to the hypothesis that the orthorhombic deformation is at the origin of the nonmodulated magnetic order. To explore that hypothesis, we examine magnetic interactions in CePdAl$_3$, assuming they follow the RKKY interaction model [19], typical for metallic systems with localized magnetic moments. Within the RKKY model, the strength and the sign of exchange interactions are determined solely by the distance between magnetic atoms, i.e., Ce-Ce pairs in this case. As described in Fig. 7(a), there are (i) four in-plane nearest neighbors to the central ion, (ii) four additional in-plane next-nearest neighbors, and (iii) eight out-of-plane next-nearest neighbors.

Considering tetragonal CePdAl$_3$ with lattice parameters $a_t = 4.37$ Å and $c_t = b = 10.4$ Å, the fourfold symmetry restricts each of (i), (ii), and (iii) as equidistant classes of neighbors, (i) at 4.37 Å, (ii) at 6.18 Å, and (iii) at 6.05 Å. With the assignment of different coupling to each class, (i) J_x^{NN}, (ii) J_x^{NNN}, and (iii) J_z^{NNN}, we examine the case of antiferromagnetic nearest-neighbor interaction J_x^{NN} as a leading term in the interaction scheme. This causes the in-plane nearest neighbors to align antiferromagnetically with respect to the central atom, but also the four out-of-plane atoms with respect to each other, as in Fig. 7(a). Then, regardless of the sign of J_z^{NNN}, the interaction between the central atom and the out-of-plane atoms is frustrated, as two pairs are aligned ferromagnetically and two others antiferromagnetically. Also, if we assume the J_z^{NNN} to be the leading term, by similar line of reasoning we arrive at the conclusion that the antiferromagnetic J_x^{NN} interaction frustrates the nearest-neighbor interactions. The in-plane, next-nearest-neighbor interaction J_x^{NNN} of ferromagnetic character is compatible with antiferromagnetic J_x^{NN}, but antiferromagnetic coupling again frustrates the system, as it competes with the nearest-neighbor interaction J_x^{NN}. Most importantly, the frustration arises independently of the orientation of the magnetic moments.

According to the RKKY model, the exchange interaction is an oscillating function of atomic distance. This allows for sig-

nificant next-nearest-neighbor interaction strength, such that the frustration contributes on a significant scale to the overall energy of the system and does not permit a collinear ground state.

Orthorhombic distortion in CePdAl$_3$ preserves the nearest-neighbor bonds, while splitting and mixing next-nearest neighbors, such that (ii) and (iii) fall within a range from 5.72 to 6.38 Å [49]. Consequently, the frustration imposed by the equivalence of out-of-plane bonds is relieved in the orthorhombic structure. This allows one to realize the arrangement exhibited by CePdAl$_3$ shown in Fig. 7(a).

Among tetragonal Ce-113 compounds, CeCuAl$_3$, CePtAl$_3$, and CeCuGa$_3$ seem to realize the antiferromagnetic nearest-neighbor interaction, based on their magnetic moments' arrangement. In the magnetically ordered state, they establish modulation of the magnetic moment amplitude with an in-plane modulation vector, $k_z = 0$, which breaks the fourfold symmetry axis and lowers the lattice symmetry from tetragonal to orthorhombic. The modulation has the amplitude of $\mu_{max} = 0.2$ μ_B in CeCuAl$_3$, 1.1 μ_B in CePtAl$_3$, and 0.67 μ_B in CeCuGa$_3$. As the crystal field reduces the magnetic moment in CePdAl$_3$ only to 1.67 μ_B from the expected $g_J J = 2.14$ μ_B for the isolated ion, further reduction of the magnetic moment amplitude in CeCuAl$_3$, CePtAl$_3$, and CeCuGa$_3$ could originate from the frustration.

In summary, the restrictions of tetragonal symmetry frustrate the magnetic interaction scheme in CePdAl$_3$ and do not allow for the long-range magnetic order. The orthorhombic distortion relieves the frustration and allows for a long-range antiferromagnetic state.

V. CONCLUSIONS

We investigated the crystal and magnetic structure of orthorhombic CePdAl$_3$ by x-ray and neutron diffraction, with further insights into crystal-field effects based on inelastic neutron scattering.

The systematic pseudotetragonal twinning of the orthorhombic lattice of CePdAl$_3$ originates from lattice deformation following the tetragonal-orthorhombic transition. The transition has its grounds in the small energy differences between tetragonal and orthorhombic phases, which allow quenching either phase, consistent with previous reports.

Orthorhombic CePdAl$_3$ establishes a collinear, antiferromagnetic type of long-range magnetic order below $T_N = 5.3$ K. The magnetic moments of the cerium atoms order along the *a* axis and form ferromagnetic sheets, stacked along the *c* axis. This type of order is consistent with single-ion anisotropies in the form of B_n^m Stevens parameters, which arise from crystal-electric field effects. The CEF scheme is fully characterized and the measured spectra are in perfect agreement with our calculations based on the determined B_n^m parameters.

We discussed the frustration mechanism based on the antiferromagnetic interaction between nearest neighbors on the tetragonal lattice, and how the orthorhombic distortion releases that frustration. We propose that this mechanism is responsible for establishing long-range magnetic order in CePdAl$_3$, as opposed to tetragonal CePdAl$_3$, where no order was observed down to 0.1 K.

[1] P. Curie, On symmetry in physical phenomena, symmetry of an electric field and of a magnetic field, J. Phys. **3**, 401 (1894).

[2] M. Shatruk, $ThCr_2Si_2$ structure type: The perovskite of intermetallics, J. Solid State Chem. **272**, 198 (2019).

[3] F. Steglich, J. Aarts, C. D. Bredl, W. Lieke, D. Meschede, W. Franz, and H. Schäfer, Superconductivity in the presence of strong Pauli paramagnetism: $CeCu_2Si_2$, Phys. Rev. Lett. **43**, 1892 (1979).

[4] E. Bauer, G. Hilscher, H. Michor, C. Paul, E. W. Scheidt, A. Gribanov, Y. Seropegin, H. Noël, M. Sigrist, and P. Rogl, Heavy fermion superconductivity and magnetic order in noncentrosymmetric $CePt_3Si$, Phys. Rev. Lett. **92**, 027003 (2004).

[5] T. Takeuchi, S. Hashimoto, T. Yasuda, H. Shishido, T. Ueda, M. Yamada, Y. Obiraki, M. Shiimoto, H. Kohara, T. Yamamoto, K. Sugiyama, K. Kindo, T. D. Matsuda, Y. Haga, Y. Aoki, H. Sato, R. Settai, and Y. Ōnuki, Magnetism and superconductivity in a heavy-fermion superconductor, $CePt_3Si$, J. Phys.: Condens. Matter **16**, L333 (2004).

[6] N. Kimura, K. Ito, K. Saitoh, Y. Umeda, H. Aoki, and T. Terashima, Pressure-induced superconductivity in noncentrosymmetric heavy-fermion $CeRhSi_3$, Phys. Rev. Lett. **95**, 247004 (2005).

[7] C. Pfleiderer, Superconducting phases of f-electron compounds, Rev. Mod. Phys. **81**, 1551 (2009).

[8] N. Egetenmeyer, J. L. Gavilano, A. Maisuradze, S. Gerber, D. E. MacLaughlin, G. Seyfarth, D. Andreica, A. Desilets-Benoit, A. D. Bianchi, Ch. Baines, R. Khasanov, Z. Fisk, and M. Kenzelmann, Direct observation of the quantum critical point in heavy fermion $CeRhSi_3$, Phys. Rev. Lett. **108**, 177204 (2012).

[9] Z. Hossain, C. Geibel, F. Weickert, T. Radu, Y. Tokiwa, H. Jeevan, P. Gegenwart, and F. Steglich, Yb-based heavy-fermion metal situated close to a quantum critical point, Phys. Rev. B **72**, 094411 (2005).

[10] T. T. M. Palstra, A. A. Menovsky, J. van den Berg, A. J. Dirkmaat, P. H. Kes, G. J. Nieuwenhuys, and J. A. Mydosh, Superconducting and magnetic transitions in the heavy-fermion system URu_2Si_2, Phys. Rev. Lett. **55**, 2727 (1985).

[11] G. R. Stewart, Non-Fermi-liquid behavior in d- and f-electron metals, Rev. Mod. Phys. **73**, 797 (2001).

[12] M. Klicpera, P. Javorský, P. Čermák, A. Schneidewind, B. Ouladdiaf, and M. Diviš, Neutron scattering study of magnetic order in single-crystalline $CeCuAl_3$, Phys. Rev. B **91**, 224419 (2015).

[13] D. T. Adroja, C. De La Fuente, A. Fraile, A. D. Hillier, A. Daoud-Aladine, W. Kockelmann, J. W. Taylor, M. M. Koza, E. Burzurí, F. Luis, J. I. Arnaudas, and A. Del Moral, Muon spin rotation and neutron scattering study of the noncentrosymmetric tetragonal compound $CeAuAl_3$, Phys. Rev. B **91**, 134425 (2015).

[14] M. Stekiel, P. Čermák, C. Franz, W. Simeth, S. Weber, E. Ressouche, W. Schmidt, K. Nemkovski, H. Deng, A. Bauer, C. Pfleiderer, and A. Schneidewind, Incommensurate antiferromagnetic order in $CePtAl_3$, Phys. Rev. Res. **5**, 013058 (2023).

[15] V. K. Anand, A. Fraile, D. T. Adroja, S. Sharma, R. Tripathi, C. Ritter, C. de la Fuente, P. K. Biswas, V. Garcia Sakai, A. del Moral, and A. M. Strydom, Crystal electric field and possible coupling with phonons in Kondo lattice $CeCuGa_3$, Phys. Rev. B **104**, 174438 (2021).

[16] N. D. Khanh, T. Nakajima, X. Yu, S. Gao, K. Shibata, M. Hirschberger, Y. Yamasaki, H. Sagayama, H. Nakao, L. Peng, K. Nakajima, R. Takagi, T. Arima, Y. Tokura, and S. Seki, Nanometric square skyrmion lattice in a centrosymmetric tetragonal magnet, Nat. Nanotechnol. **15**, 444 (2020).

[17] R. Takagi, N. Matsuyama, V. Ukleev, L. Yu, J. S. White, S. Francoual, J. R. L. Mardegan, S. Hayami, H. Saito, K. Kaneko, K Ohishi, Y. Ōnuki, T. Arima, Y. Tokura, T. Nakajima, and S. Seki, Square and rhombic lattices of magnetic skyrmions in a centrosymmetric binary compound, Nat. Commun. **13**, 1472 (2022).

[18] K. W. H. Stevens, Matrix elements and operator equivalents connected with the magnetic properties of rare earth ions, Proc. Phys. Soc. A **65**, 209 (1952).

[19] J. H. Van Vleck, Note on the interactions between the spins of magnetic ions or nuclei in metals, Rev. Mod. Phys. **34**, 681 (1962).

[20] A. D. Hillier, D. T. Adroja, P. Manuel, V. K. Anand, J. W. Taylor, K. A. McEwen, B. D. Rainford, and M. M. Koza, Muon spin relaxation and neutron scattering investigations of the noncentrosymmetric heavy-fermion antiferromagnet $CeRhGe_3$, Phys. Rev. B **85**, 134405 (2012).

[21] V. K. Anand, A. D. Hillier, D. T. Adroja, D. D. Khalyavin, P. Manuel, G. Andre, S. Rols, and M. M. Koza, Understanding the magnetism in noncentrosymmetric $CeIrGe_3$: Muon spin relaxation and neutron scattering studies, Phys. Rev. B **97**, 184422 (2018).

[22] M. Smidman, D. T. Adroja, A. D. Hillier, L. C. Chapon, J. W. Taylor, V. K. Anand, R. P. Singh, M. R. Lees, E. A. Goremychkin, M. M. Koza, V. V. Krishnamurthy, D. M. Paul, and G. Balakrishnan, Neutron scattering and muon spin relaxation measurements of the noncentrosymmetric antiferromagnet CeCoGe$_3$, Phys. Rev. B **88**, 134416 (2013).

[23] C. Franz, A. Senyshyn, A. Regnat, C. Duvinage, R. Schönmann, A. Bauer, Y. Prots, L. Akselrud, V. Hlukhyy, V. Baran, and C. Pfleiderer, Single crystal growth of CeTAl$_3$ ($T=$ Cu, Ag, Au, Pd and Pt), J. Alloys Compd. **688**, 978 (2016).

[24] C. Schank, F. Jährling, L. Luo, A. Grauel, C. Wassilew, R. Borth, G. Olesch, C. D. Bredl, C. Geibel, and F. Steglich, $4f$-conduction electron hybridization in ternary Ce-TM-Al compounds, J. Alloy Compd. **207**, 329 (1994).

[25] V. Kumar, A. Bauer, C. Franz, J. Spallek, R. Schönmann, M. Stekiel, A. Schneidewind, M. A. Wilde, and C. Pfleiderer, Low-temperature antiferromagnetic order in orthorhombic CePdAl$_3$, Phys. Rev. Res. **5**, 023157 (2023).

[26] A. Neubauer, J. Bœuf, A. Bauer, B. Russ, H. V. Löhneysen, and C. Pfleiderer, Ultra-high vacuum compatible image furnace, Rev. Sci. Instrum. **82**, 013902 (2011).

[27] A. Bauer, G. Benka, A. Regnat, C. Franz, and C. Pfleiderer, Ultra-high vacuum compatible preparation chain for intermetallic compounds, Rev. Sci. Instrum. **87**, 113902 (2016).

[28] *Agilent,* Crysalis^{Pro} *Software System, ver. 1.171.36.28*, (Agilent Technologies UK Ltd., Oxford, UK, 2013).

[29] H. M.-L. Zentrum, DNS: Diffuse scattering neutron time-of-flight spectrometer, JLSRF **1**, A27 (2015).

[30] W. Schweika and P. Böni, The instrument DNS: Polarization analysis for diffuse neutron scattering, Physica B **297**, 155 (2001).

[31] A. Boothroyd, *Principles of Neutron Scattering from Condensed Matter* (Oxford University Press, Oxford, 2020).

[32] O. Arnold, J. C. Bilheux, J. M. Borreguero, A. Buts, S. I. Campbell, L. Chapon, M. Doucet, N. Draper, R. Ferraz Leal, M. A. Gigg, V. E. Lynch, A. Markvardsen, D. J. Mikkelson, R. L. Mikkelson, R. Miller, K. Palmen, P. Parker, G. Passos, T. G. Perring, P. F. Peterson, S. Ren, M. A. Reuter, A. T. Savici, J. W. Taylor, R. J. Taylor, R. Tolchenov, W. Zhou, and J. Zikovsky, Mantid-Data analysis and visualization package for neutron scattering and μSR experiments, Nucl. Instrum. Methods Phys. Res. Sect. A **764**, 156 (2014).

[33] H. M.-L. Zentrum, HEiDi: Single crystal diffractometer at hot source, JLSRF **1**, A7 (2015).

[34] V. Petříček, M. Dušek, and L. Palatinus, Crystallographic computing system JANA2006: General features, Zeit. Kristallogr. **229**, 345 (2014).

[35] B. Fåk, S. Rols, G. Manzin, and O. Meulien, Panther - The new thermal neutron time-of-flight spectrometer at the ILL, EPJ Web Conf. **272**, 02001 (2022).

[36] G. Kresse and J. Furthmüller, Efficiency of *ab initio* total energy calculations for metals and semiconductors using a plane-wave basis set, Comput. Mater. Sci. **6**, 15 (1996).

[37] J. P. Perdew, K. Burke, and M. Ernzerhof, Generalized gradient approximation made simple, Phys. Rev. Lett. **77**, 3865 (1996).

[38] T. Atsushi and T. Isao, First principles phonon calculations in materials science, Scr. Mater. **108**, 1 (2015).

[39] D. Legut, U. D. Wdowik, and P. Kurtyka, Vibrational and dielectric properties of $\alpha-$Si$_3$N$_4$ from density functional theory, Mater. Chem. Phys. **147**, 42 (2014).

[40] M. Stekiel, CRYSFIPY: Crystal-field Hamiltonian analysis in PYTHON, https://github.com/mstekiel/crysfipy.

[41] P. Čermák, J. Zubáč, and K. Pajskr, CRYSFIPY: Crystal field suite for PYTHON, https://bitbucket.org/cermak/crysfipy/src/master/.

[42] K. R. Andress and E. Alberti, Roentgenographische Untersuchung der Legierungsreihe Al-Ba, Z. Metallkd. **27**, 126 (1935).

[43] W. H. Press, S. A. Teukolsky, W. T. Vetterling, and B. P. Flannery, *Numerical recipes, The Art of Scientific Computing* (Cambridge University Press, Cambridge, 2007).

[44] M. Loewenhaupt, B. D. Rainford, and F. Steglich, Dynamic jahn-teller effect in a rare-earth compound: CeAl$_2$, Phys. Rev. Lett. **42**, 1709 (1979).

[45] D. T. Adroja, A. del Moral, C. de la Fuente, A. Fraile, E. A. Goremychkin, J. W. Taylor, A. D. Hillier, and F. Fernandez-Alonso, Vibron quasibound state in the noncentrosymmetric tetragonal heavy-fermion compound CeCuAl$_3$, Phys. Rev. Lett. **108**, 216402 (2012).

[46] P. Čermák, A. Schneidewind, Be. Liu, M.-M. Koza, C. Franz, R. Schönmann, O. Sobolev, and C. Pfleiderer, Magnetoelastic hybrid excitations in CeAuAl$_3$, Proc. Natl. Acad. Sci. USA **116**, 6695 (2019).

[47] V. Chlan, P. Doležal, R. Sgallová, M. Klicpera, C. Franz, and P. Javorský, Local atomic arrangement in LaCuAl$_3$ and LaAuAl$_3$ by NMR and density functional theory, J. Phys.: Condens. Matter **31**, 385601 (2019).

[48] S. Nallamuthu, A. Dzubinska, M. Reiffers, J. Rodriguez-Fernandez, and R. Nagalakshmi, Ferromagnetism in orthorhombic RAgAl$_3$ ($R =$ Ce and Pr) compounds, Physica B **521**, 128 (2017).

[49] Orthorhombic distortion splits the 4×6.18 Å in-plane, next-nearest neighbor (NNN) into 2×5.97 Å (FM) and 2×6.38 Å (FM) neighbors, while the 8×6.05 Å out-of-plane NNN is split into 2×5.72 Å (AF), 4×6.1 Å (FM), and 2×6.28 Å (AF).

[50] M. Stekiel, P. Čermák, B. Fåk, C. Franz, U. B. Hansen, M. M. Koza, and A. Schneidewind, Magnetoelastic coupling of crystal field transitions and lattice excitations in CePdAl$_3$, Institut Laue-Langevin, 2021, doi: 10.5291/ILL-DATA.DIR-254.